Acta Materialia 259 (2023) 119223

Contents lists available at ScienceDirect

Acta Materialia

journal homepage: www.elsevier.com/locate/actamat

Full length article

Room temperature plasticity in amorphous SiO_2 and amorphous Al_2O_3: A computational and topological study

Jiahui Zhang [a,b,*], Erkka J. Frankberg [b], Janne Kalikka [c], Antti Kuronen [a]

[a] Department of Physics, University of Helsinki, Gustaf Hällströmin katu 2, 00014, Helsinki, Finland
[b] Materials Science and Environmental Engineering Unit, Tampere University, Korkeakoulunkatu 6, Tampere, 33720, Finland
[c] Physics Unit, Tampere University, Korkeakoulunkatu 6, Tampere, 33720, Finland

ARTICLE INFO

Keywords:
Molecular dynamics simulations
Amorphous oxides
Plastic deformation

ABSTRACT

Requirements for room temperature plasticity in oxides glasses have been only recently established. While atomistic mechanisms of this type of plasticity have been reported, it remains challenging to translate this knowledge between different structures and predict what other oxide glasses can be ductile and by which principle. Here we show that a coarse-grained analysis at the polyhedral level gives valuable information to accompany the atomistic characterization of plasticity, and we propose the analysis of *polyhedral neighbor change events (PNCE)* as a tool to allow comparison of the room temperature plasticity in various oxide glasses. Classical atomistic simulations with around 1 million atoms provided primitive data for coarse-grained analysis. Based on the PNCE analysis, the edge-sharing polyhedra are found to be up to 2 orders of magnitude more active in enabling plasticity, and combined with the occurrence of edge-sharing polyhedra, is shown to explain the brittle to ductile transition in a-SiO_2 and the intrinsically high ductility of a-Al_2O_3. Finally, the coarse-grained analysis enables the benefit of using additional topological constraint theory analysis to yield more in-depth information regarding the ductile features of each glass structure. Quantitative comparison between amorphous Al_2O_3 and SiO_2 shows a consistent trend between the materials and shows that the approach can be extended to the designing of other damage tolerant oxide glass materials.

1. Introduction

Oxide glasses are widely used today in many fields because of their excellent electrical, optical and chemical properties [1–3]. However, these materials are commonly known to be brittle [4,5], and this weakness limits their wider usage. The brittleness stems from the fact that the ionic and covalent bonds in oxide glasses are rigid and cannot be switched as easily as in metals [6,7]. However, there are exceptions to this brittleness. Amorphous aluminum oxide (a-Al_2O_3) is a known semiconductor substrate material and a network modifier material in glass materials design. Recently it was shown that thin, 40–60 nm, films of a-Al_2O_3 can permanently deform without fracture at room temperature and under unconfined tensile and shear loading, and that the plasticity extends theoretically to the bulk scale [8]. In addition, plasticity in a-Al_2O_3 is known to be possible under confined indentation [9], or when the size of the material specimen is reduced to extreme nanoscale [10]. Plastic deformation at low temperature is known to occur in amorphous metal alloys, i.e., metallic glasses. It is currently understood to be induced mainly by shear flow leading to the formation of shear bands [11]. Although similar processes are active during the plasticity of a-Al_2O_3 [8], the low-temperature plasticity of oxide glasses remains a less understood phenomenon. In contrast to a-Al_2O_3, amorphous SiO_2 (a-SiO_2) is a strong glass former widely used in our daily life [12]. Together, oxides of Al and Si can form binary cation systems with important usages in ceramic science and technology [13]. Glassy a-SiO_2 is generally known to be a brittle material, but atomistic simulations have shown that a brittle to ductile (BTD) transition can be artificially induced in a-SiO_2. For example, by simulating a high hydrostatic pressure during the melt quenching step, a-SiO_2 can be significantly densified. As a result, the densified structure can endure plastic strain without fracture during molecular dynamics (MD) mechanical simulations even at room temperature [14,15]. Besides the differences in initial structures, BTD transition can be induced in a-SiO_2 by conducting tensile tests at different strain rates, straining conditions, and temperature, or using different shapes of the samples [16]. However, it is essential to note that the ductility can be an artefact created by certain simulation conditions that should be avoided [17,18].

* Corresponding author at: Department of Physics, University of Helsinki, Gustaf Hällströmin katu 2, 00014, Helsinki, Finland.
E-mail address: jiahui.zhang@helsinki.fi (J. Zhang).

https://doi.org/10.1016/j.actamat.2023.119223
Received 15 March 2023; Received in revised form 2 August 2023; Accepted 5 August 2023
Available online 9 August 2023

One mechanism proposed to explain the plasticity in densified a-SiO_2 is the competition between the formation energies of shear-bands and cleavage in the system. In densified a-SiO_2, forming of a shear-band is preferred to forming a cleavage because of its lower formation energy, so that the system deforms in such a manner to avoid fracture [19]. On the atomistic level, Yuan and Huang [14] found that in densified a-SiO_2, bond switching events are more likely to occur around the newly formed 5-fold Si atoms. The system can dissipate stored elastic energy and endure higher strain by bond switching *i.e.*, breaking and reforming their bonds around these sites [20].

5-fold Si atoms only exist in densified a-SiO_2 but 5-fold Al atoms are common in a-Al_2O_3 [21]. It is known that the non-densified a-SiO_2 structure is a network of SiO_4 tetrahedra connected with each other via shared corner atoms. The a-Al_2O_3 has a similar but more compact network formed by AlO_n polyhedra, with n ranging between 4 to 6. Such a similarity, owing to the cation-centered polyhedral structure, allows us to compare these two materials to gain insight into what enables low temperature plasticity in oxide glasses. For example, their mechanical behavior can be analyzed based on changes in the polyhedron coordination and a medium-range order at the polyhedral level, allowing a more coarse-grained comparison not currently available in the literature.

Based on the coarse-grained analysis, we also apply the Topological Constraint Theory (TCT) to gain further insight into the plasticity mechanism found in densified a-SiO_2 and a-Al_2O_3. TCT has been successfully used to predict glass forming ability and design novel SiO_2 based glass materials [22]. For example, TCT guided the design of a glass type used in modern smartphone screens [23]. TCT has proven to be a powerful tool in capturing the universal characteristics of amorphous materials directly from their coarse-grained topological structure rather than the atomic properties of their composition. For example, in calcium silicate glass, it was found that when quenched at different temperatures, the system always attempts to reach an isostatic status [24], having a topological constraint of three, as first suggested by Maxwell [25]. When applying TCT on the fracture toughness of glasses, BTD transition was also observed in calcium silicate glasses. When this system changed from under constrained to isostatic, its fracture behavior changed and the stress curve transitioned from purely brittle to slightly ductile [26]. Based on this example, and despite TCT has so far been mainly used to study the effect of the composition of the glasses, here we attempt to analyze whether TCT can predict any of the critical features of plasticity between densified a-SiO_2 and a-Al_2O_3.

By studying the fundamental mechanism behind plasticity, we can have a deeper understanding on how to design new damage tolerant glass materials. In this work, we use the molecular dynamics method to simulate the tensile deformation of non-densified and densified a-SiO_2 and non-densified a-Al_2O_3 as a comparison. The hypothesis is that in addition to the BTD transition, increasing the density of a-SiO_2 causes an increase in edge-sharing polyhedra fraction approaching that of a-Al_2O_3, which is an intrinsically more ductile oxide glass material. As a result, plasticity observed in densified a-SiO_2 and a-Al_2O_3 is shown to correlate to the same coarse-grained structural parameters, giving valuable information regarding the origin of both room temperature plasticity in oxide glasses. In addition, the results explain why some oxide glass materials remain brittle. Further, comparing the plasticity reveals the dislocation mechanism required for the BTD transition in a-SiO_2 at a polyhedral coarse-grained level. Finally, we apply TCT-based analysis on these structures to explain further why plasticity exists in some of these glass systems. Results show that bond-bending constraint value is not always positively correlated to the spatial density of bonds in the material.

2. Methods

2.1. Preparation of amorphous structures

For a-SiO_2, the potential developed by van Beest et al. (BKS) [27] is used in this study. This partial charge potential of Buckingham form has been proved capable of reproducing the density, Young's modulus, and melting points of SiO_2 correctly [28]. To prevent the instability at short interatomic distances, the BKS potential is truncated at short range and replaced by a harmonic repulsive part, as proposed by Vollmayr et al. [29]. For Al_2O_3, the Buckingham potential parameterization developed by Matsui [30] is used. It is known to describe well the liquid and a-states Al_2O_3 [8]. Molecular dynamics simulations are performed using the LAMMPS code [31] and analyzed using OVITO analysis and visualization software [32].

A-Al_2O_3 and a-SiO_2 are prepared from rectangular shape corundum and quartz structures, respectively. Sufficiently large system sizes are chosen to avoid any finite size effects [18]. For a-Al_2O_3, the simulation box size is $11 \times 11 \times 90$ nm^3 with around 1,000,000 atoms (see Fig. S1). The same cast quench method as in Ref. [33] is used to get the initial structure for the tensile tests. The Nosé-Hoover thermostat and barostat implemented in LAMMPS are used for temperature and pressure control. The system is first melted in 5000 K in NVT at a density of 2.75 g/cm^3, then cooled down to 3000 K in 10 ps and equilibrated in NVT ensemble. Density is changed to 3.175 g/cm^3 during equilibrium and cooled to 300 K at a cooling rate of 3.6 K/ps. Afterward, the structure is annealed at 300 K and 1 atmosphere in NPT ensemble to produce the final structure. For a-SiO_2, an $11 \times 11 \times 85$ nm^3 system containing about 800,000 atoms is prepared similarly as a-Al_2O_3 (see Fig. S2). The system is heated up to 5000 K and equilibrated first, then slowly cooled down in NPT ensemble, using similar procedure mentioned by Luo [28]. To completely erase the original structure and avoid the structure's influence at the liquid phase, a cooling rate of 1 K/ps is used. Hydrostatic pressure from 0 to 8 GPa is applied to obtain the densified samples during cast quenching. The pressure is applied to the system when the temperature reaches 5000 K, and removed from the system when the system is relaxed at 300 K.

2.2. Tensile test simulations

Structures obtained from the last step of the above-mentioned preparations are then used in tensile tests. A strain rate of 5×10^8 s^{-1} is used in all the tensile test simulations and strained to a maximum of 50% elongation. The tensile force is applied along the long axis of the simulation system to avoid the artificial ductility and other size effects seen in previous works [17]. The system is kept at 300 K and zero pressure with NPT ensemble in directions orthogonal to the elongation. The simulation box is deformed every timestep (1 fs) without remapping the atomic positions. To clarify, in all the following figures we used engineering strain ϵ which is defined as

$$\epsilon = \frac{L - L_0}{L_0}, \tag{1}$$

where L_0 and L are the original length of the system and the current momentary lengths measured after a degree of deformation, respectively.

2.3. Characterization of the structures

For topological analysis, polyhedra constructed by a center Si or Al atom and its bonded O atoms are treated as a basic structural element of the system. Oxygen atoms that are within a specific cutoff distance from the center atom are considered as bonded. Cutoff distance is taken to be the first minimum of the radial distribution function, i.e., 2.3 Å for a-Al_2O_3 and 2.1 Å for a-SiO_2. Two polyhedra with at least one shared O atom are considered polyhedral neighbors. If a polyhedron has all its bonded O atoms shared with different neighboring polyhedra, it is a corner-sharing polyhedron (CSph). If a polyhedron has two shared O atoms with any of its neighbors, it is an edge-sharing polyhedron (ESph) (see Fig. 1(a) for illustration). Polyhedra with more than two shared O atoms with their neighbor are rare and were not included in our analysis.

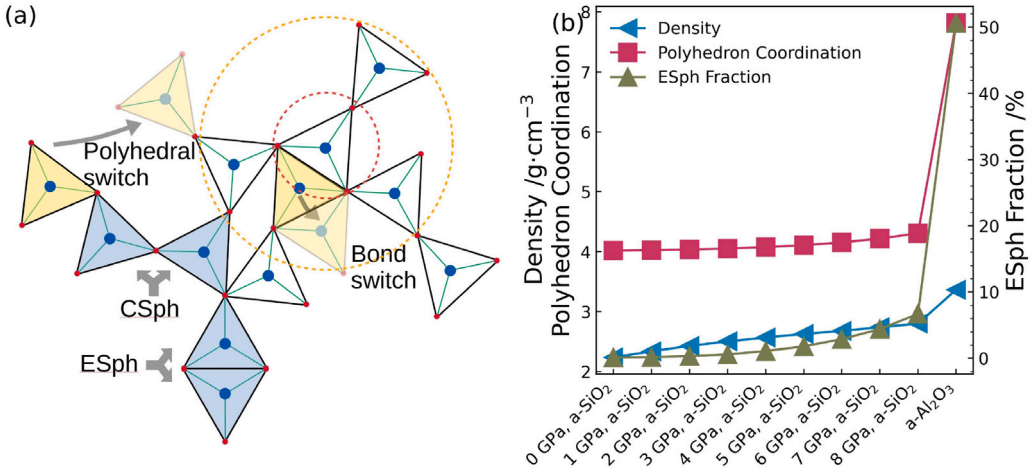

Fig. 1. (a) 2-D schematic of oxide glass polyhedra with different topological status. Cation atoms are colored blue, oxygen atoms are colored red, cation–oxygen bonds are shown as blue lines, and black lines are the edges of fictive polyhedra. Edge-sharing polyhedra and corner-sharing polyhedra are distinguishable in this figure. Polyhedral neighbor change and bond change are illustrated with arrows. The red dashed-line circle indicates the scale of information conveyed by bond switching analysis, i.e. the scale of individual atom bonds (short-range order), and the yellow dashed-line circle indicates information that coarse-grained analysis could reveal, i.e., the scale of neighboring polyhedra. (b) Density, polyhedron coordination, and ESph fraction of a-SiO_2 that quenched at different pressures and a-Al_2O_3. (For interpretation of the references to color in this figure legend, the reader is referred to the web version of this article.)

D^2_{min} is the minimum value of the square of the local atomic displacement (D^2) and describes the local deviation from affine deformation compared to a reference configuration, as introduced by Falk and Langer [34]. It is a descriptor of local plastic strain and is used to capture plastic deformation during tensile tests. In this study, we use momentary D^2_{min} to characterize the plastic events in the simulated samples. A 1% strain interval between the reference configuration and the configuration to be analyzed is used. The cutoff distance decides the range within which the atomic configurations would be compared. To make results comparable, cutoff distance in D^2_{min} calculation is set to 2× r_{min}, where r_{min} is the first minimum on the radial distribution function. For a-Al_2O_3 and a-SiO_2, these cutoffs are 4.6 Å and 4.2 Å, respectively.

Similar to the calculation of atomic coordination number, polyhedron coordination is the number of polyhedra that have shared oxygen with the central polyhedron. Compared to the atomic coordination number, this is expected to give more information about the medium-range order of the system. For each polyhedron, a polyhedral neighbor change event (PNCE) is defined as the change of the polyhedron neighbors between a reference and the current configuration. It is calculated as the exclusive disjunction of the polyhedral neighbor list between reference and current configuration, the strain increment between these two adjacent configurations ($\Delta\varepsilon$) is 0.05%.

We categorize the PNCEs into four possible cases between two adjacent configurations and two polyhedra types. To compare the occurrence of these different PNCE types, we count each PNCE with a CSph involved and each PNCE with ESph involved. The counted PNCE is normalized by dividing the number of the corresponding type of polyhedron (N_{CSph}, N_{ESph}), and then divided again by the increment in strain ($\Delta\varepsilon$) to produce a time-independent result, given as

$$P_{CSph} = \frac{PNCE^{CSph}_{ESph} + PNCE^{ESph}_{CSph} + PNCE^{CSph}_{CSph}}{N_{CSph}\Delta\varepsilon} \quad (2)$$

$$P_{ESph} = \frac{PNCE^{ESph}_{CSph} + PNCE^{CSph}_{ESph} + PNCE^{ESph}_{ESph}}{N_{ESph}\Delta\varepsilon}, \quad (3)$$

where P is the normalized number of events per $\Delta\varepsilon$ strain change, $PNCE^{CSph}$ means it is a CSph before the event, $PNCE_{ESph}$ means it is an ESph after the event, $\Delta\varepsilon$ is the strain increment between two adjacent configurations, and N_{CSph} means the total number of CSph type polyhedra after the increment.

To gain further insight into the origin of room temperature plasticity, bond bending constraints (n_c^{BB}) related to TCT were used to determine the stability of the polyhedra on an atomic level. n_c^{BB} is the angular bond-bending constraints that keep the bond angles fixed around their average values. The values of the O–Si–O, and O–Al–O bond angles are continuously enumerated over time based on molecular dynamics simulations. A time period equivalent to 1% strain (20 ps) is treated as quasi-static for constraint evaluation. We then calculate each bond angle over time and the standard deviation (σ) of bond angles. If the standard deviation is smaller than the given threshold value, which means the excursion of the bond angle is small enough, the bond angle would be considered an active constraint of the center atom. Different threshold values are used to compute bond-bending constraints from standard deviation distributions and probe the stability of the bond angles.

3. Results

3.1. Quenched samples

The density, fraction of edge-sharing polyhedra and average polyhedra coordination of the simulated structures are presented in Fig. 1(b). In SiO_2 samples, density changes from 2.25 g/cm^3 to 3.05 g/cm^3 when the quenching pressure varies from 0 to 8 GPa. This indicates a strong ability to densify, which has also been observed experimentally [35]. While a-Al_2O_3 quenched at ambient pressure (0 GPa) intrinsically produces a 44.4% and 6.6% denser structure compared to a-SiO_2 quenched under 0 GPa and 8 GPa pressure, respectively. It has been reported in previous work that for 0 GPa quenched a-SiO_2, nearly all oxygen atoms bonded to silicon atoms are bridging oxygen atoms (BO) [36,37], consistent with our results that only negligible amount of non-bridging oxygen (NBO) atoms are observed (see Fig. S3). For most crystalline phases of SiO_2, the basic structural element of the system is a tetrahedron formed by one 4-fold coordinated Si center atom and four 2-fold coordinated O corner atoms. SiO_4 tetrahedron also acts as the basic structural element of amorphous SiO_2. The difference is that, in the amorphous phase, the tetrahedra are connected with each other more arbitrarily, as indicated by the bond angle distribution of Si-O-Si bonds [38,39]. ESph fraction results in Fig. 1(b) show that, for 0 GPa a-SiO_2, tetrahedra of the system are mostly connected with each other by sharing one corner oxygen atom. But when the pressure increases, the edge-sharing polyhedra take a greater fraction. At 8 GPa, ESph

Table 1
Correlation between atomic coordination and polyhedron types in the 0 and 8 GPa a-SiO_2 and a-Al_2O_3 (in percentage). A negligible amount of CN < 4 polyhedra are observed only in 0 GPa SiO_2.

Coordination	a-SiO_2, 0 GPa		a-SiO_2, 8 GPa		a-Al_2O_3	
	CSph	ESph	CSph	ESph	CSph	ESph
CN = 4	99.6	0.1	90.4	0.4	42.8	18.8
CN > 4	0.3	0.0	2.9	6.3	1.5	37.0

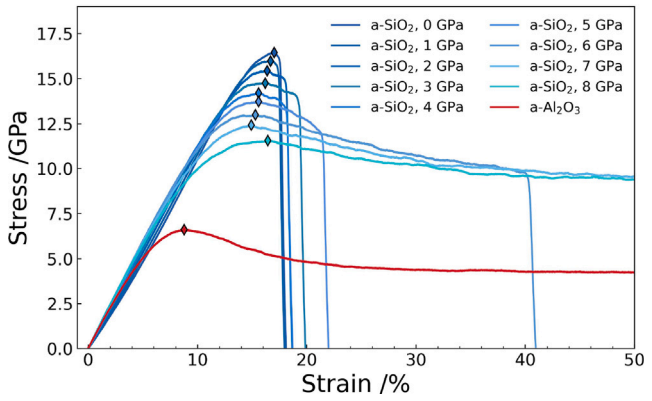

Fig. 2. Stress as a function of strain for a-Al_2O_3 and for a-SiO_2 structures quenched at different pressures as obtained from 0%–50% strain tensile test simulations. The ultimate stress points of structures are marked with diamond markers.

fraction increased from 0% in 0 GPa a-SiO_2 to 7%. However, this value is still much lower when compared to a-Al_2O_3 which has more than 50% of its polyhedra structures edge-sharing with each other, even without any pressure applied during quenching (see Table 1). Fig. 1(b) also shows average polyhedron coordination from 4.0 to 4.4 for a-SiO_2 systems and 7.9 for a-Al_2O_3. Compared to atomic coordination reported by others [29,40], polyhedron coordination number shows a significant difference between a-SiO_2 and a-Al_2O_3 which is not shown as clearly in the coordination number distribution of atoms and shows how the coarse-grained, polyhedral based, approach can yield additional information.

3.2. Tensile tests

Tensile test simulations are performed with obtained initial structures. Fig. 2 shows the stress–strain curves for all simulated systems. We can see that 0 GPa a-SiO_2 shows almost pure brittle behavior, but as the sample gets denser with increasing quench pressure, the ultimate strength decreases and fracture strain increases. Brittle a-SiO_2 shows minor yielding before fracture. However, as quenching pressure increases from 0 to 6 GPa, a-SiO_2 structures show clearer yielding before fracture. At 7–8 GPa, the quenched sample can endure 50% strain without fracture. A BTD transition occurred for a-SiO_2, indicating the plasticity increase in the densified structures. In comparison, a-Al_2O_3 behaves in a ductile manner and has a much lower ultimate stress which correlates with the lower strain required to initiate yielding compared to a-SiO_2. As we observe a trend of decreasing yield stress as a function of increasing density, we can compare it to the mechanical behavior of crystals. In crystals, the lowest critical resolved shear stress and the coinciding dislocation slip typically occurs along the close-packed atom planes with the highest number of atoms per area [41]. We propose that in an isotropic amorphous oxide, the overall increase in density can similarly lead to a decrease in the ultimate stress needed to dislocate the tetrahedra and atoms. The occurrence of plastic strain is further confirmed by doing offloading simulations, which verifies the occurrence of permanent elongation (see Fig. S4).

3.3. Characterization of strained structures

To reveal more details regarding plastic behaviors, the results from tensile tests are characterized in multiple ways. Fig. 3 shows density, the fraction of edge-sharing polyhedra, average polyhedron coordination, and average momentary D^2_{min} as functions of strain. We use the ultimate stress point to divide the results into two parts, showing a clear difference between the low and high-strain parts. Before the ultimate stress, we see from Fig. 3(a) that the density of all the structures decreases with strain. For a-Al_2O_3, the density levels after ultimate stress, while in a-SiO_2, the density keeps decreasing up to 50% strain. The decreasing density under stress can result from one or more mechanisms, such as plastic viscous creep leading to changes in local structure and coordination or the appearance of new cavities in the system (see Fig. S6). Fig. 3(b) shows the momentary D^2_{min} averaged over all atoms as a function of strain during tensile tests. In 0 GPa a-SiO_2, the increment occurs just before the ultimate stress and fracture and and are probably correlated to forming and propagating of the fracture surface. But in densified SiO_2, the gradual increment of D^2_{min} between the start and ultimate stress point is earlier and smoother. It shows that densified a-SiO_2 responds faster to the increase of stress, with more active local plasticity, and the sensitivity is positively correlated to increasing quenching pressure.

Further analyses are performed on a coarse-grained scale to add topological information about the systems here. We analyze the polyhedron coordination number change as a function of strain as presented in Fig. 3(c). We can see the decrease of polyhedron coordination number with strain before the ultimate stress, indicating that the decrease of density is partly due to the decrease of polyhedron coordination, *i.e.* medium-range order change. Decreased polyhedron coordination can also result from CSph and ESph configuration changes. Fig. 3(d) shows that the ESph fraction decreased in all structures before the ultimate stress point. Together the data in Fig. 3(c–d) indicates that structures with plastic stress–strain correlation show plasticity not only after the ultimate stress point, but an increased number of mobile atoms even at the elasto-plastic phase of the stretching before ultimate stress. For densified SiO_2, the decrement of ESph fraction in Fig. 3(d) is more significant than that of 0 GPa a-SiO_2, similar to Fig. 3(c). For a-Al_2O_3, the ESph fraction is much higher in general, but the variance is comparable with the 8 GPa a-SiO_2 and shows a similar trend of recovering ESph fraction after ultimate stress.

To study the correlation between ESph fraction change and localized rearrangement of atoms, and moreover, plasticity in the structures, a coarse-grained neighbor change analysis is performed on the structures, namely the PNCE, to characterize how active different kinds of polyhedra are during tensile tests. As presented in Fig. 4, we see that in 0 GPa quenched a-SiO_2, the polyhedra in the system, practically all tetrahedra, have very low PNCE, which means that they barely change their polyhedral neighbors during stretching. While as the system becomes more densified, the neighbor-changing ability of polyhedra gradually increases. In 8 GPa quenched a-SiO_2, the number of polyhedral neighbor change events is significantly larger than 0 GPa quenched SiO_2. The total number of PNCE is an indicator of how active the polyhedra structure is during stretching, and it gives consistent results with the visualization results (see Movie S1-S10) in which a-SiO_2 is a very rigid framework and 8 GPa a-SiO_2, a-Al_2O_3 are more flexible. These results are consistent with the previous results on atom bond switching data on a-Al_2O_3 and a-SiO_2 [8,28].

PNCE is categorized and presented in Fig. 5. As mentioned, ESph fraction increased from 0% to about 7%, from 0 GPa quenched SiO_2 to 8 GPa quenched SiO_2. From Fig. 5, the results further show that ESph is involved in about 30% of the total number of PNCEs in the case of 8 GPa a-SiO_2, but in a negligible amount in 0 GPa a-SiO_2. Results for 8 GPa a-SiO_2 indicate that each ESph contributes roughly four times more to the localized rearrangement of atoms than CSph. Besides the fraction difference, the total number of PNCE in a-Al_2O_3 is

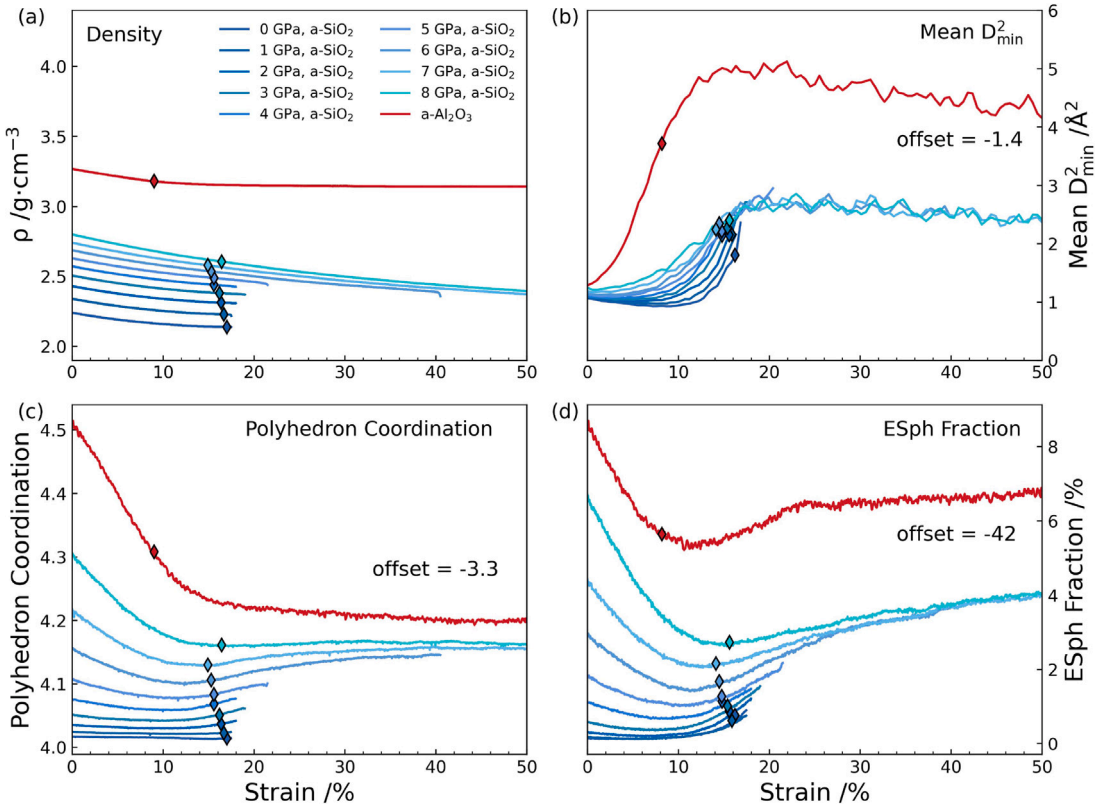

Fig. 3. Various structural characteristics as a function of strain during the tensile test for a-SiO_2 quenched at 0 to 8 GPa and for a-Al_2O_3. Diamond markers show the ultimate stress point of each structure. (a) Density. (b) Mean momentary D^2_{min}. (c) Polyhedron coordination. (d) Fraction of edge-sharing polyhedra. Note that the curves for a-Al_2O_3 are offset vertically by the shown amount.

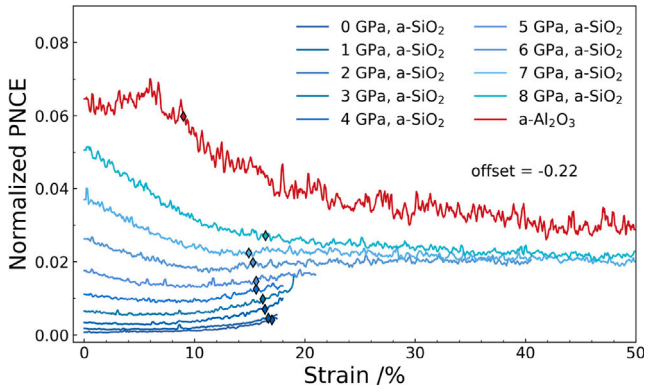

Fig. 4. Average polyhedron neighbor change events (PNCE) as a function of strain. Results for a-Al_2O_3 has been offset to allow comparison with others. The diamond marker shows the ultimate stress point of each structure.

two orders of magnitude higher than that in 0 GPa a-SiO_2, indicating a much more active system during tensile test simulations (see Movie S10). Because ESph composes a share of up to 7% of all polyhedra in densified a-SiO_2, in Fig. 6 we calculated the normalized number of events per $\Delta\varepsilon$ strain change (P) in such a way that the PNCE data in Fig. 5 is divided by the total number of the corresponding type of polyhedron and increment of strain, as given in Eqs. (2) and (3). Results represent the activity of each type of polyhedron and are presented in Fig. 6. They clearly show that although ESph only composes a minor or even negligible fraction in normal and densified a-SiO_2, it is many times more active in changing its polyhedral neighbors than CSph. The activity difference between ESph and CSph is around twice in a-Al_2O_3, but increases to over two hundred times in 0 GPa a-SiO_2. Moreover, from 0 GPa to 8 GPa densified a-SiO_2, CSph also becomes more active. Since the calculation involves the transition between ESph and CSph, the increase of CSph activity P in a-SiO_2 structures is partly because ESph is also involved, and their fraction is increasing. These results prove that ESph contributes more to the localized rearrangement of atoms than what would be anticipated based on their substantially smaller fraction. To exclude the error induced by different fracture strains, the strain ranges of 2%, 1% before and after the ultimate stress, is selected to get a time-averaged normalized PNCE, and obtained results are compared between structures in Fig. 7. The difference in P between ESph and CSph changes from 2.2, for 0 GPa a-SiO_2, to 4.4 for 8 GPa a-SiO_2, and for a-Al_2O_3 the difference is 2.2. A significant difference between corner-sharing and edge-sharing polyhedra proves that the ESph mediates plasticity much more actively than the CSph. In a-Al_2O_3, the ESph is more active than CSph, but the difference is not as significant as in SiO_2. Quantitative analysis results reveal that ESph contributes to localized rearrangements related to plasticity by more frequent polyhedral neighbor changing. This change does not only include swapping between ESph and ESph but also includes a transition between ESph and CSph.

We then investigate how different ESph and CSph are during tensile tests. Convex hull volume of polyhedra with 4-fold and 5-fold center cations are computed for a-Al_2O_3 and 8 GPa a-SiO_2. The probability density functions of the volume are presented in Figs. 8(a)(b). Results at 0 and 50% strain are shown with lighter and darker curves for comparison. Here the total area under the distribution curve is the fraction of each polyhedron type. Volume distribution has a narrower peak for polyhedra with 4-fold center atoms than those with 5-fold center atoms, which means that 4-fold tetrahedra have a more rigid structure than other polyhedra. Their number also shows minor changes before and after the tensile test since the area under the curve does not change much. For polyhedra with the 5-fold center atom, the volume between

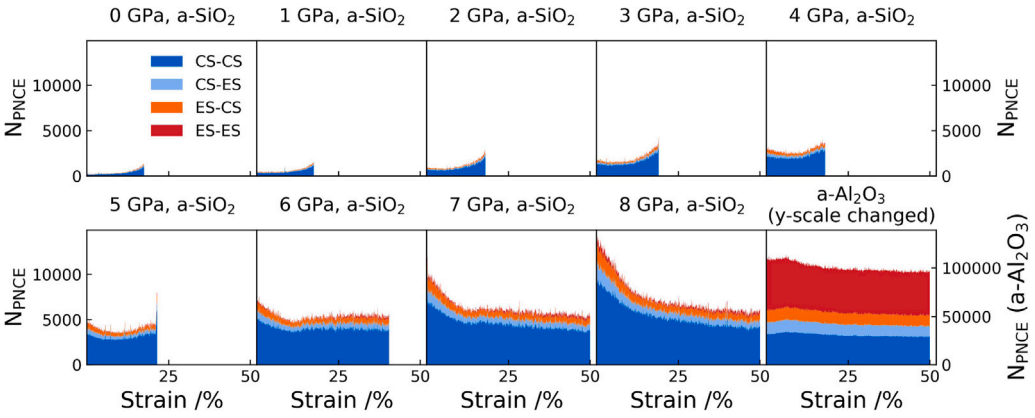

Fig. 5. Types of polyhedral neighbor change events (PNCE) in all structures during the tensile test, where the x-axis is the engineering strain in percentage, the y-axis indicates the PNCE number. Four different types of PNCE are shown as different colors, given in the legend.

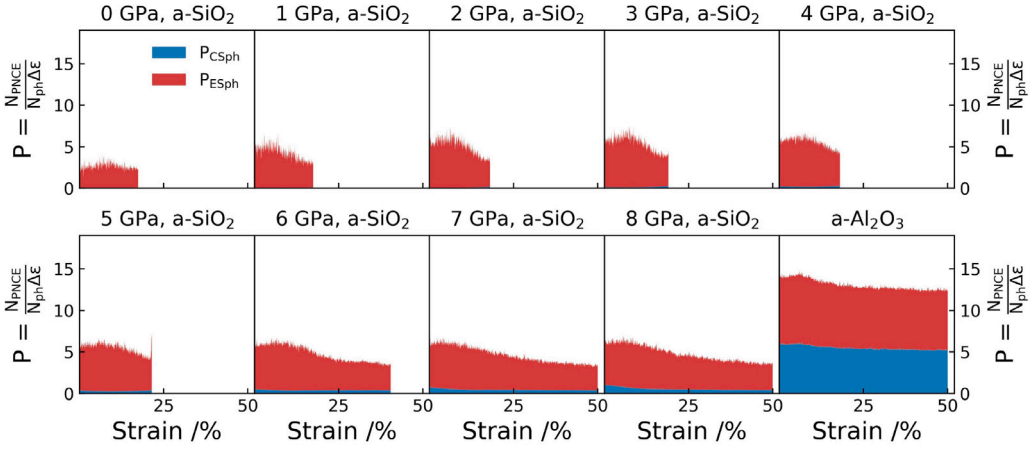

Fig. 6. Normalized number of events per $\Delta\epsilon$ strain change for CSph and ESph polyhedra in all structures during stretching, where the x-axis is the engineering strain in percentage, the y-axis indicates how active each type of polyhedron is quantified using Eqs. (2) and (3).

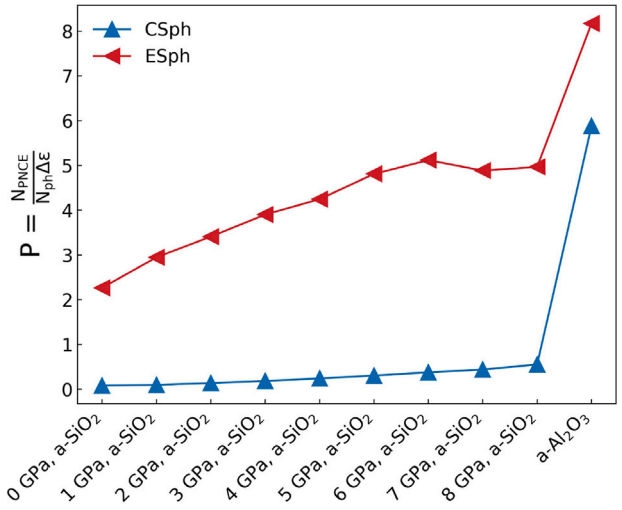

Fig. 7. Normalized number of events per $\Delta\epsilon$ strain change for CSph and ESph polyhedra. in all structures at the ultimate stress. Y-axis indicates the probability of polyhedral neighbor change events quantified using Eqs. (2) and (3) but only on the 2% strain range around the ultimate stress point to compare between structures. X-axis indicates different amorphous structures.

0 and 50% strain shows a clear difference in both a-Al_2O_3 and 8 GPa a-SiO_2. Hence we can conclude that during deformation, polyhedra with 4-fold center atoms are relatively more stable than that with 5-fold center atoms.

As one of the two types of constraints introduced by topological constraint theory (TCT), bond bending constraints (n_c^{BB}) are computed during tensile tests for all systems. A dynamic bond-bending constraint results of structures n_c^{BB} are shown in Fig. 8(c). An active bond bending constraint is a bond angle that is stable enough during the selected period of time. In practice, it means that the bond angle values in that period of time have a standard deviation smaller than a given threshold value, denoted as σ_θ. By changing σ_θ, it is possible to probe the distribution of the standard deviation and, additionally, the bond angles of the whole system and get a general indicator of how rigid the network of the system is. In this work, we have picked three σ_θ values for the calculation of n_c^{BB}: σ_θ=7°, 15° and 80°. σ_θ=15° is used as the threshold value in other works to check whether a constraint is active, but σ_θ=7° would only include bond angles that oscillate within a narrow range. While σ_θ=80° is a large value and was picked here to include most of the bond angles despite the changing of their value during a given period of time, as the ceiling of the n_c^{BB} in this work. In Fig. 8(c), results show that for 0 GPa SiO_2, σ_θ=15° is indeed a proper threshold value to check whether a bond angle is stable or not. The reason is that the value of n_c^{BB} increased obviously from 7° to 15°, but does not change from 15° to 80°, indicating that all the bond angles are included with σ_θ=15°. Results are consistent with our earlier results that 0 GPa SiO_2 has a very rigid structure, and the bonds in the system are very stable in a time scale of 1 ns (see Movie S1). But for densified SiO_2, as quenching pressure increases, n_c^{BB} computed with σ_θ = 15°

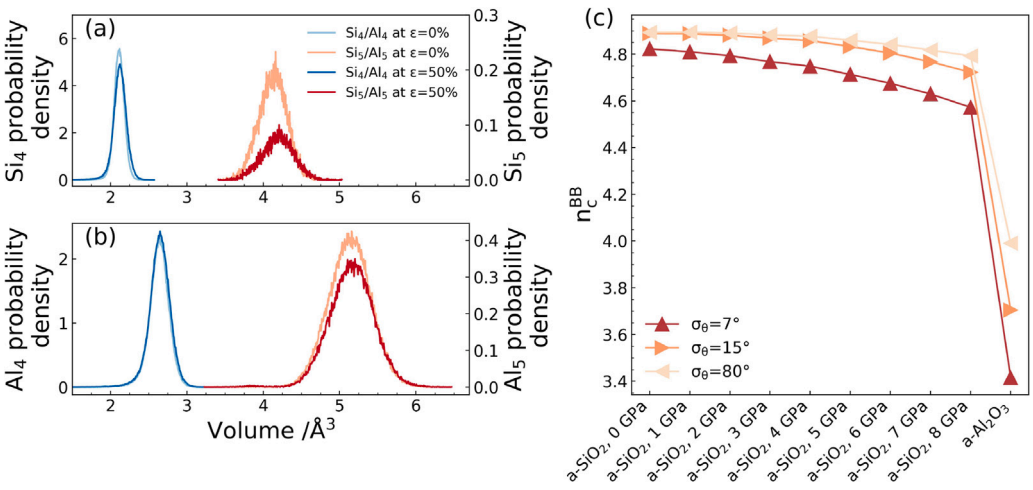

Fig. 8. (a)(b) Volume change of polyhedra with the 4-fold and 5-fold center atom in 8 GPa quenched a-SiO_2 (a) and a-Al_2O_3 (b) between 0 (lighter solid line) and 50 (darker solid line) % strain. N(V) indicates the polyhedra number in each bin, *i.e.* 4-fold Al N(V) indicates the number of polyhedra that have 4-fold Al as their center atoms at the corresponding volume, the difference between light and the dark line is the difference between 0% and 50% strain. *X*-axis indicates different amorphous structures. (c) Bond-bending constraints per atom for different initial structures. *Y*-axis is the value of bond-bending constraints per atom. σ_θ is the standard deviation threshold to determine if a bond angle is an active constraint. (For interpretation of the references to color in this figure legend, the reader is referred to the web version of this article.)

and $\sigma_\theta = 80°$ start to separate. This means that more variation in bond angles is allowed as part of the bond angles now drop from the range of 15° to 80°, unlike in the more stable 0 GPa SiO_2. The trend of calculated n_c^{BB} is decreasing, which indicates a changing from narrower to a broader range of possible bond angles and more flexible bonds. For a-Al_2O_3, there are large differences with different threshold values, indicating a wider distribution of standard deviation and more unstable bond angles in the system.

4. Discussion

To understand why a-SiO_2 and a-Al_2O_3 quenched at normal pressure are so different regarding mechanical properties, we must first understand their structural differences occurring before the tensile tests. It is better to mention B_2O_3, a widely used oxide glass material similar to SiO_2. SiO_2 and B_2O_3 meet all the prerequisites proposed by Zachariasen that a glass former should meet [42] since the most common crystalline phases of B_2O_3 and SiO_2 are formed by periodic network of BO_3 triangles and SiO_4 tetrahedra respectively. They are the stable structural elements of these two materials in crystalline and amorphous phases. Whether they are forming a uniform or a random network decides the occurring phase of the system [4]. On the other hand, a-Al_2O_3 is an unconventional glass material that needs specific techniques to prepare. It is known that in corundum (α-Al_2O_3), Al and O atoms have coordination numbers of 6 and 4, respectively [43]. But when the quench of liquid Al_2O_3 is simulated at very high cooling rates, the obtained amorphous structure has Al atoms that are mostly (90%) 4-fold and 5-fold coordinated, as shown in Table 1. A significant difference in the structural elements between crystalline and amorphous phase partly explains why it is harder for a-Al_2O_3 to be prepared.

Fracture in oxide glass materials has been analyzed energetically as the competition between fracture surface energy and stored elastic energy [17]. From an energetic perspective, the increase of fracture strain in a-SiO_2 as quenching pressure increases is partly because densified a-SiO_2 dissipated more energy at early strain and delayed the formation of the fracture surface (See Fig. S5). As a-SiO_2 gets denser, more energy is required to form fracture surfaces.

Quantifying plasticity and comparing the characterization between different oxide glass materials has been challenging. A nowadays widely used method is the D^2_{min} analysis to capture the localized deformation [34]. It does show a clear difference between brittle (0 GPa a-SiO_2) and ductile (8 GPa a-SiO_2) materials and similar spatial distribution in the two ductile materials (8 GPa a-SiO_2, a-Al_2O_3), as shown in Fig. S8. However, quantification shows that significant differences still exist between ductile materials, as mean D^2_{min} shows. The fact that D^2_{min} is sensitive to cutoff and coordination of the system makes comparison between materials difficult. In Fig. 4, we tried to quantify the plastic activity of the system using PNCE, because it also characterizes the structure based on medium-range order and is not very sensitive to bond length. PNCE represents the polyhedral level activity and is more comparable between different systems.

In Figs. 6 and 7 we show that edge-sharing polyhedra are more active during stretching. Therefore, our main hypothesis based on coarse-grained analysis is that edge-sharing polyhedra are more active during deformation, and the increase of their number as the quenching pressure increases is why BTD transition happens in a-SiO_2. To compare coarse-grained analysis results to atomic level analysis results, Yuan and Huang proposed that 5-fold Si atoms are more active during tensile tests of a-SiO_2 [14]. Here we show that in densified SiO_2, a significant fraction of the 5-fold Si atoms is also the center atoms of the ESph (Table 1), and a wider volume distribution in Fig. 8(a) also proves the edge-sharing polyhedra are more flexible than corner-sharing polyhedra. Coarse-grained level analysis broadens our understanding of the plasticity mechanism: Frankberg et al. found that for 0 GPa a-SiO_2 and a-Al_2O_3, bond switching analysis showed that a-Al_2O_3 has 8 to 25 times more active bond switching [8]. However, on a coarse-grained level, we found that the actual difference might be even more significant. In Fig. 4 the PNCE of 0 GPa a-SiO_2 is two orders of magnitude lower than that of a-Al_2O_3. Therefore, atomistic and coarse-grained analyses should be made to characterize the low temperature plasticity of other oxide glasses better.

We can make a more meaningful comparison between materials with coarse-grained analysis using polyhedral-level systemic information. For example, in a binary alumino-silicate system, it has been found that the system is getting more ductile with a higher Al_2O_3 ratio [44]. The bond length change between cation and oxygen atoms in a binary system makes D^2_{min} analysis inconsistent. However, with the coarse-grained method, we can assume that the rise of Al_2O_3 content changes the topological structure and then induces ductility. Additionally, even if the polyhedral level coarse-grained analysis results might be convenient for understanding the plastic behaviors of materials, we cannot neglect the intrinsic difference on the atomic level, as we wanted to show with the polyhedral volume change and bond-bending constraint analysis shown in Fig. 8. By checking the volume change of different

types of polyhedra, we notice that the volume change of tetrahedra during stretching is more minor compared to 5-fold polyhedra, indicating that the tetrahedra are more rigid. Different from analytical TCT results that are derived from the average coordination number of the system, by evaluating each bond angle we prove that densified a-SiO_2 and a-Al_2O_3 have lower bond bending constraints despite having more bonds per atom. This supports our results that the stable tetrahedra network will no longer exist when the system gets denser. It contains more edge-sharing polyhedra, making the system less stable and advocating bond switching and PNCEs, leading to potential plasticity even at room temperature.

5. Conclusions

Tensile test simulations have been performed at room temperature for a-SiO_2 structures quenched at different pressures and for a-Al_2O_3 structures. Results show that the plasticity of a-SiO_2 increases when the system has more edge-sharing polyhedra (ESph). As the number fraction of ESph increases with quenching pressure, a-SiO_2 can endure higher strain without fracture. To compare, a-Al_2O_3 is highly ductile, and we show it to have a much higher edge-sharing polyhedra fraction than the densified a-SiO_2. Our analysis reveals that ESph is much more active during stretching in all of the studied oxide glass systems than corner-sharing polyhedra (CSph), contributing a more prominent part to localized rearrangement of atoms and plastic deformation ability than their number fraction in the system would indicate. A higher share of ESph in a-Al_2O_3 leads to 2 orders of magnitude higher polyhedral neighbor change event (PNCE) activity related to plasticity. Quantitative coarse-grained comparison between the plasticity of a-Al_2O_3 and a-SiO_2 shows a consistent trend despite their different short-range atomic properties such as bond length and cation/oxygen ratio. The results indicate that analysis of polyhedra neighbor change events in combination with Topological Constraint Theory provides a valuable tool to design damage tolerant oxide glass materials.

Declaration of competing interest

The authors declare that they have no known competing financial interests or personal relationships that could have appeared to influence the work reported in this paper.

Acknowledgments

We acknowledge funding from the Academy of Finland project numbers 315451, 315453, 326426, 338750 and 332347. The computational resources granted by the CSC – IT Center for Science projects 2003839 (LAPLAS Glass Plasticity at Room Temperature) and hy3898, Finland, and by the Finnish Grid and Cloud Infrastructure project (FGCI; urn:nbn:fi:research-infras-2016072533) are gratefully acknowledged.

Appendix A. Supplementary data

Supplementary material related to this article can be found online at https://doi.org/10.1016/j.actamat.2023.119223.

References

[1] Y. Idota, T. Kubota, A. Matsufuji, Y. Maekawa, T. Miyasaka, Tin-based amorphous oxide: A high-capacity lithium-ion-storage material, Science 276 (1997) 1395–1397, http://dx.doi.org/10.1126/science.276.5317.1395, URL https://www.science.org/doi/10.1126/science.276.5317.1395.

[2] J. Kim, S. Kim, H.-H. Lee, K. Lee, W. Ma, X. Gong, A. Heeger, New architecture for high-efficiency polymer photovoltaic cells using solution-based titanium oxide as an optical spacer, Adv. Mater. 18 (2006) 572–576, http://dx.doi.org/10.1002/adma.200501825, URL https://onlinelibrary.wiley.com/doi/10.1002/adma.200501825.

[3] G. Karbasian, M. McConnell, H. George, L. Schneider, M. Filmer, A. Orlov, A. Nazarov, G. Snider, Metal-insulator-metal single electron transistors with tunnel barriers prepared by atomic layer deposition, Appl. Sci. 7 (2017) 246, http://dx.doi.org/10.3390/app7030246, URL http://www.mdpi.com/2076-3417/7/3/246.

[4] A.K. Varshneya, Fundamentals of Inorganic Glasses, Elsevier, 2013.

[5] Z. Yin, F. Hannard, F. Barthelat, Impact-resistant nacre-like transparent materials, Science 364 (2019) 1260–1263, http://dx.doi.org/10.1126/science.aaw8988, URL https://www.science.org/doi/10.1126/science.aaw8988.

[6] L. Wondraczek, Overcoming glass brittleness, Science 366 (2019) 804–805, http://dx.doi.org/10.1126/science.aaz2127, URL https://www.science.org/doi/10.1126/science.aaz2127.

[7] L. Wondraczek, J.C. Mauro, J. Eckert, U. Kühn, J. Horbach, J. Deubener, T. Rouxel, Towards ultrastrong glasses, Adv. Mater. 23 (2011) 4578–4586, http://dx.doi.org/10.1002/adma.201102795, URL https://onlinelibrary.wiley.com/doi/10.1002/adma.201102795.

[8] E.J. Frankberg, J. Kalikka, F.G. Ferré, L. Joly-Pottuz, T. Salminen, J. Hintikka, M. Hokka, S. Koneti, T. Douillard, B.L. Saint, P. Kreiml, M.J. Cordill, T. Epicier, D. Stauffer, M. Vanazzi, L. Roiban, J. Akola, F.D. Fonzo, E. Levänen, K. Masenelli-Varlot, Highly ductile amorphous oxide at room temperature and high strain rate, Science 366 (2019) 864–869, http://dx.doi.org/10.1126/science.aav1254, 1. Why they didn't mention the potential used in their simulation?, URL https://www.science.org/doi/10.1126/science.aav1254.

[9] F.G. Ferré, E. Bertarelli, A. Chiodoni, D. Carnelli, D. Gastaldi, P. Vena, M.G. Beghi, F.D. Fonzo, The mechanical properties of a nanocrystalline Al2O3/a-Al2O3 composite coating measured by nanoindentation and brillouin spectroscopy, Acta Mater. 61 (2013) 2662–2670, http://dx.doi.org/10.1016/j.actamat.2013.01.050, URL https://linkinghub.elsevier.com/retrieve/pii/S1359645413000797.

[10] Y. Yang, A. Kushima, W. Han, H. Xin, J. Li, Liquid-like, self-healing aluminum oxide during deformation at room temperature, Nano Lett. 18 (2018) 2492–2497, http://dx.doi.org/10.1021/acs.nanolett.8b00068, URL https://pubs.acs.org/doi/10.1021/acs.nanolett.8b00068.

[11] A. Argon, Plastic deformation in metallic glasses, Acta Metall. 27 (1979) 47–58, http://dx.doi.org/10.1016/0001-6160(79)90055-5, URL https://linkinghub.elsevier.com/retrieve/pii/0001616079900555.

[12] C.A. Angell, Formation of glasses from liquids and biopolymers, Science 267 (5206) (1995) 1924–1935, URL http://www.jstor.org/stable/2886440.

[13] H. Morikawa, S.-I. Miwa, M. Miyake, F. Marumo, T. Sata, Structural analysis of SiO2-Al2O3 glasses, J. Am. Ceram. Soc. 65 (1982) 78–81, http://dx.doi.org/10.1111/j.1151-2916.1982.tb10361.x, URL https://onlinelibrary.wiley.com/doi/10.1111/j.1151-2916.1982.tb10361.x.

[14] F. Yuan, L. Huang, Brittle to ductile transition in densified silica glass, Sci. Rep. 4 (2014) 5035, http://dx.doi.org/10.1038/srep05035, URL https://www.nature.com/articles/srep05035.

[15] J.M.D. Lane, Cooling rate and stress relaxation in silica melts and glasses via microsecond molecular dynamics, Phys. Rev. E 92 (2015) 012320, http://dx.doi.org/10.1103/PhysRevE.92.012320, URL https://link.aps.org/doi/10.1103/PhysRevE.92.012320.

[16] F. Yuan, L. Huang, Size-dependent elasticity of amorphous silica nanowire: A molecular dynamics study, Appl. Phys. Lett. 103 (2013) 201905, http://dx.doi.org/10.1063/1.4830038, URL https://pubs.aip.org/aip/apl/article/130059.

[17] F. Yuan, L. Huang, Molecular dynamics simulation of amorphous silica under uniaxial tension: From bulk to nanowire, J. Non-Cryst. Solids 358 (2012) 3481–3487, http://dx.doi.org/10.1016/j.jnoncrysol.2012.05.045, URL https://linkinghub.elsevier.com/retrieve/pii/S0022309312003602.

[18] Z. Zhang, S. Ispas, W. Kob, The critical role of the interaction potential and simulation protocol for the structural and mechanical properties of sodosilicate glasses, J. Non-Cryst. Solids 532 (2020) http://dx.doi.org/10.1016/j.jnoncrysol.2020.119895.

[19] Y. Shi, J. Luo, F. Yuan, L. Huang, Intrinsic ductility of glassy solids, J. Appl. Phys. 115 (2014) http://dx.doi.org/10.1063/1.4862959, URL https://pubs.aip.org/jap/article/115/4/043528/345242/Intrinsic-ductility-of-glassy-solids.

[20] Y.-C. Chen, Z. Lu, K. ichi Nomura, W. Wang, R.K. Kalia, A. Nakano, P. Vashishta, Interaction of voids and nanoductility in silica glass, Phys. Rev. Lett. 99 (2007) 155506, http://dx.doi.org/10.1103/PhysRevLett.99.155506, URL https://link.aps.org/doi/10.1103/PhysRevLett.99.155506.

[21] T. Du, H. Liu, L. Tang, S.S. Sørensen, M. Bauchy, M.M. Smedskjaer, Predicting fracture propensity in amorphous alumina from its static structure using machine learning, ACS Nano 15 (2021) 17705–17716, http://dx.doi.org/10.1021/acsnano.1c05619, URL https://pubs.acs.org/doi/10.1021/acsnano.1c05619.

[22] M. Bauchy, Deciphering the atomic genome of glasses by topological constraint theory and molecular dynamics: A review, Comput. Mater. Sci. 159 (2019) 95–102, http://dx.doi.org/10.1016/j.commatsci.2018.12.004.

[23] P. Ball, Concrete mixing for gorillas, Nature Mater. 14 (5) (2015) 472, http://dx.doi.org/10.1038/nmat4279.

[24] M. Bauchy, M. Micoulaut, Densified network glasses and liquids with thermodynamically reversible and structurally adaptive behaviour, Nature Commun. 6 (2015) 6398, http://dx.doi.org/10.1038/ncomms7398, URL https://www.nature.com/articles/ncomms7398.

[25] J.C. Maxwell, On the calculation of the equilibrium and stiffness of frames, The London, Edinburgh, and Dublin Philosophical Magazine and Journal of Science 27 (182) (1864) 294–299, http://dx.doi.org/10.1080/14786446408643668, arXiv:10.1080/14786446408643668.

[26] M. Bauchy, B. Wang, M. Wang, Y. Yu, M.J.A. Qomi, M.M. Smedskjaer, C. Bichara, F.-J. Ulm, R. Pellenq, Fracture toughness anomalies: Viewpoint of topological constraint theory, Acta Mater. 121 (2016) 234–239, http://dx.doi.org/10.1016/j.actamat.2016.09.004, URL https://linkinghub.elsevier.com/retrieve/pii/S1359645416306838.

[27] B.W.H. van Beest, G.J. Kramer, R.A. van Santen, Force fields for silicas and aluminophosphates based on ab initio calculations, Phys. Rev. Lett. 64 (1990) 1955–1958, http://dx.doi.org/10.1103/PhysRevLett.64.1955, URL https://link.aps.org/doi/10.1103/PhysRevLett.64.1955.

[28] J. Luo, J. Wang, E. Bitzek, J.Y. Huang, H. Zheng, L. Tong, Q. Yang, J. Li, S.X. Mao, Size-dependent brittle-to-ductile transition in silica glass nanofibers, Nano Lett. 16 (2016) 105–113, http://dx.doi.org/10.1021/acs.nanolett.5b03070, URL https://pubs.acs.org/doi/10.1021/acs.nanolett.5b03070.

[29] K. Vollmayr, W. Kob, K. Binder, Cooling-rate effects in amorphous silica: A computer-simulation study, Phys. Rev. B 54 (1996) 15808–15827, http://dx.doi.org/10.1103/PhysRevB.54.15808, URL https://link.aps.org/doi/10.1103/PhysRevB.54.15808.

[30] M. Matsui, A transferable interatomic potential model for crystals and melts in the system CaO-MgO-Al2O3-SiO2, Mineral. Mag. 58A (1994) 571–572, http://dx.doi.org/10.1180/minmag.1994.58A.2.34.

[31] A.P. Thompson, H.M. Aktulga, R. Berger, D.S. Bolintineanu, W.M. Brown, P.S. Crozier, P.J. in 't Veld, A. Kohlmeyer, S.G. Moore, T.D. Nguyen, R. Shan, M.J. Stevens, J. Tranchida, C. Trott, S.J. Plimpton, LAMMPS - a flexible simulation tool for particle-based materials modeling at the atomic, meso, and continuum scales, Comput. Phys. Comm. 271 (2022) 108171, http://dx.doi.org/10.1016/j.cpc.2021.108171.

[32] A. Stukowski, Visualization and analysis of atomistic simulation data with OVITO-the open visualization tool, Model. Simul. Mater. Sci. Eng. 18 (1) (2010) http://dx.doi.org/10.1088/0965-0393/18/1/015012.

[33] G. Gutiérrez, B. Johansson, Molecular dynamics study of structural properties of amorphous Al2O3, Phys. Rev. B 65 (2002) 104202, http://dx.doi.org/10.1103/PhysRevB.65.104202, URL https://link.aps.org/doi/10.1103/PhysRevB.65.104202.

[34] M.L. Falk, J.S. Langer, Dynamics of viscoplastic deformation in amorphous solids, Phys. Rev. E 57 (1998) 7192–7205, http://dx.doi.org/10.1103/PhysRevE.57.7192, URL https://link.aps.org/doi/10.1103/PhysRevE.57.7192.

[35] M. Murakami, S. Kohara, N. Kitamura, J. Akola, H. Inoue, A. Hirata, Y. Hiraoka, Y. Onodera, I. Obayashi, J. Kalikka, N. Hirao, T. Musso, A.S. Foster, Y. Idemoto, O. Sakata, Y. Ohishi, Ultrahigh-pressure form of Si O2 glass with dense pyrite-type crystalline homology, Phys. Rev. B 99 (4) (2019) 045153, http://dx.doi.org/10.1103/PhysRevB.99.045153.

[36] R. Dupree, D. Holland, P. McMillan, R. Pettifer, The structure of soda-silica glasses: A mas NMR study, J. Non-Cryst. Solids 68 (1984) 399–410, http://dx.doi.org/10.1016/0022-3093(84)90020-6, URL https://linkinghub.elsevier.com/retrieve/pii/0022309384900206.

[37] J. Du, A. Cormack, The medium range structure of sodium silicate glasses: a molecular dynamics simulation, J. Non-Cryst. Solids 349 (2004) 66–79, http://dx.doi.org/10.1016/j.jnoncrysol.2004.08.264, URL https://linkinghub.elsevier.com/retrieve/pii/S0022309304007963.

[38] J. Neuefeind, K.-D. Liss, Bond angle distribution in amorphous germania and silica, Ber. Bunsenges. Phys. Chem. 100 (1996) 1341–1349, http://dx.doi.org/10.1002/bbpc.19961000812, URL https://onlinelibrary.wiley.com/doi/10.1002/bbpc.19961000812.

[39] X. Yuan, A. Cormack, Si–o–si bond angle and torsion angle distribution in vitreous silica and sodium silicate glasses, J. Non-Cryst. Solids 319 (2003) 31–43, http://dx.doi.org/10.1016/S0022-3093(02)01960-9, URL https://linkinghub.elsevier.com/retrieve/pii/S0022309302019609.

[40] H. Hashimoto, Y. Onodera, S. Tahara, S. Kohara, K. Yazawa, H. Segawa, M. Murakami, K. Ohara, Structure of alumina glass, Sci. Rep. 12 (2022) 1–9, http://dx.doi.org/10.1038/s41598-021-04455-6.

[41] T.H. Courtney, Mechanical Behavior of Materials, 2000.

[42] W.H. Zachariasen, The atomic arrangement in glass, J. Am. Chem. Soc. 54 (1932) 3841–3851, http://dx.doi.org/10.1021/ja01349a006, URL https://pubs.acs.org/doi/abs/10.1021/ja01349a006.

[43] T.J. Godin, J.P. LaFemina, Atomic and electronic structure of the corundum (a-alumina) (0001) surface, Phys. Rev. B 49 (1994) 7691–7696, http://dx.doi.org/10.1103/PhysRevB.49.7691, URL https://link.aps.org/doi/10.1103/PhysRevB.49.7691.

[44] J. Luo, K.D. Vargheese, A. Tandia, J.T. Harris, J.C. Mauro, Structural origin of intrinsic ductility in binary aluminosilicate glasses, J. Non-Cryst. Solids 452 (2016) 297–306, http://dx.doi.org/10.1016/j.jnoncrysol.2016.09.010.